

# Large resistivity in numerical simulations of radially self-similar outflows

M. Čemeljić<sup>1\*</sup>, N. Vlahakis<sup>2</sup>, K. Tsinganos<sup>2</sup>

<sup>1</sup>*Academia Sinica Institute of Astronomy and Astrophysics & Theoretical Institute for Advanced Research in Astrophysics, P.O. Box 23-141, Taipei 10617, Taiwan*

<sup>2</sup>*IASA and Section of Astrophysics, Astronomy and Mechanics, Department of Physics, University of Athens, Panepistemiopolis 15784 Zografos, Athens, Greece*

Received/Accepted

## ABSTRACT

We investigate the differences between an outflow in a highly-resistive accretion disk corona, and the results with smaller or vanishing resistivity. For the first time, we determine conditions at the base of a two-dimensional radially self-similar outflow in the regime of very large resistivity. We performed simulations using the PLUTO magnetohydrodynamics code, and found three modes of solutions. The first mode, with small resistivity, is similar to the ideal-MHD solutions. In the second mode, with larger resistivity, the geometry of the magnetic field changes, with a “bulge” above the super-fast critical surface. At even larger resistivities, the third mode of solutions sets in, in which the magnetic field is no longer collimated, but is pressed towards the disk. This third mode is also the final one: it does not change with further increase of resistivity. These modes describe topological change in a magnetic field above the accretion disk because of the uniform, constant Ohmic resistivity.

**Key words:** stars: pre-main sequence – magnetic fields – MHD – ISM: jets and outflows

## 1 INTRODUCTION

Outflows of plasma in the vicinity of objects from stellar to galactic scales have been observed, and are an essential ingredient in theoretical models. The energy and angular momentum transport in any such system will most certainly be affected by outflows. Their impact on the interstellar medium is huge, and is probably part of the mechanism for recycling stellar matter into new stars.

Because of computational difficulties, numerical simulations with an increasing number of physical parameters can not go much beyond the self-similar approach of, for example, Blandford & Payne (1982). This approach has been systematized in Vlahakis & Tsinganos (1998) and Vlahakis et al. (2000) into a general scheme for self-similar outflows, with two sets of exact MHD outflow models, radially and meridionally self-similar.

Simulations in Gracia et al. (2006) confirmed the stationarity of such a solution in the complete physical domain of a radially self-similar corona of a disk in the ideal-MHD approach. In Čemeljić et al. (2008)(hereafter C08), we reported an extension of radially self-similar numerical simulations in the resistive-MHD simulations using the NIRVANA

code by Ziegler (1998). There we investigated the regime of small resistivity, and reported the existence of apparent *critical magnetic diffusivity*, where the departure of the outflow shape from the ideal-MHD case stops following the trend found for small physical resistivities. Because of the long run-times of such simulations with the non-parallel NIRVANA (v.2) code, we could not proceed to investigate the large resistivity regime.

Before we can indulge in the modeling of the anomalous magnetic diffusivity in simulations instead of using the uniform diffusivity, the eventual existence of its critical value has to be resolved. This will then set the upper limit in models of resistivity, which could otherwise be difficult to prescribe in the ramifications of a particular model.

We introduce our setup, now with the parallel PLUTO code. Next we check for the influence of numerical resistivity, and then address our results in the regime of large resistivity, as compared to the trend found in simulations with small resistivity. We then discuss possible consequences of our results for astrophysical simulations.

## 2 PROBLEM SETUP

We use a similar set of initial conditions as in C08, but now using the PLUTO (v. 3.1.1) code with the parallel option

\* E-Mail: miki@tiara.sinica.edu.tw (MČ)

(Mignone et al. 2007). Here we give only a short review, for particulars we refer the reader to Gracia et al. (2006) and C08.

In SI units, the equations we solve are:

$$\frac{\partial \rho}{\partial t} + \nabla \cdot (\rho \mathbf{V}) = 0, \quad (1)$$

$$\rho \left[ \frac{\partial \mathbf{V}}{\partial t} + (\mathbf{V} \cdot \nabla) \mathbf{V} \right] + \nabla p + \rho \nabla \Phi - \frac{\nabla \times \mathbf{B}}{\mu_0} \times \mathbf{B} = 0, \quad (2)$$

$$\frac{\partial \mathbf{B}}{\partial t} - \nabla \times (\mathbf{V} \times \mathbf{B} - \eta \nabla \times \mathbf{B}) = 0, \quad (3)$$

$$\rho \left[ \frac{\partial e}{\partial t} + (\mathbf{V} \cdot \nabla) e \right] + p(\nabla \cdot \mathbf{V}) - \frac{\eta}{\mu_0} (\nabla \times \mathbf{B})^2 = 0, \quad (4)$$

$$\nabla \cdot \mathbf{B} = 0, \quad (5)$$

with  $\rho$  and  $p$  for the density and pressure,  $\mathbf{V}$  and  $\mathbf{B}$  for the velocity and magnetic field, and  $\Phi = -\mathcal{G}\mathcal{M}/r$  as the gravitational potential of the central mass  $\mathcal{M}$ . The internal energy (per unit mass) is  $e = p/(\rho(\gamma - 1))$ , where  $\gamma$  is the effective polytropic index, set to 1.05 on our simulations. The magnetic diffusivity  $\eta$  in the SI system of units is related to the electrical resistivity  $\eta_r = \mu_0 \eta$ , where  $\mu_0$  is the permeability of vacuum. In cgs units,  $\mu_0 = 1$  and  $\eta_r = \eta$ , so that in the text we will often refer to  $\eta$  as a resistivity, except when it could produce a misunderstanding.

## 2.1 Initial and boundary conditions

We used the self-similar solution of Vlahakis et al. (2000) as the initial and boundary conditions in the simulations. For steady-state, axisymmetric and radially self-similar solutions we can write, in a form with mixed spherical ( $r, \theta, \phi$ ) and cylindrical ( $Z = r \cos \theta, R = r \sin \theta, \phi$ ) coordinates:

$$\frac{\rho}{\rho_0} = \alpha^{x-3/2} \frac{1}{M^2}, \quad \frac{p}{p_0} = \alpha^{x-2} \frac{1}{M^{2\gamma}}, \quad (6)$$

$$\frac{B_p}{B_0} = -\alpha^{\frac{x}{2}-1} \frac{1}{G^2} \frac{\sin \theta}{\cos(\psi + \theta)} (\cos \psi \hat{R} + \sin \psi \hat{Z}), \quad (7)$$

$$\frac{V_p}{V_0} = -\alpha^{-1/4} \frac{M^2}{G^2} \frac{\sin \theta}{\cos(\psi + \theta)} (\cos \psi \hat{R} + \sin \psi \hat{Z}), \quad (8)$$

$$\frac{B_\phi}{B_0} = -\lambda \alpha^{\frac{x}{2}-1} \frac{1-G^2}{G(1-M^2)}, \quad \frac{V_\phi}{V_0} = \lambda \alpha^{-1/4} \frac{G^2 - M^2}{G(1-M^2)}, \quad (9)$$

where  $\alpha = \frac{R^2}{R_0^2 G^2}$ , ( $M, G, \psi$ ) are functions of  $\theta$ , and

$$V_0 = \frac{1}{\kappa} \sqrt{\frac{\mathcal{G}\mathcal{M}}{R_0}}, \quad \rho_0 = \frac{B_0^2}{\mu_0 V_0^2}, \quad p_0 = \mu \frac{B_0^2}{2\mu_0}. \quad (10)$$

The index  $p$  denotes poloidal, and the index  $\phi$  toroidal components.

The density and pressure are related by a polytropic relation  $p = Q(\alpha)\rho^\gamma$ , with the entropy function  $Q(\alpha)$  constant along a flow line, but differing from one flow line to the other. This relation is the general steady state solution of Eq. (4) in the ideal-MHD case (without the last term) for the equation of state used here,  $p/rho = e/(\gamma - 1)$ . This procedure reduces the system of ideal-MHD equations to three first-order ordinary differential equations with respect to the functions ( $G, M, \Psi$ ). A particular solution is given by the set of formal solution parameters  $(x, \lambda^2, \mu, \kappa, \gamma) = (0.75, 136.9, 2.99, 2, 1.05)$  and a prescription for the solution functions ( $G, M, \Psi$ ) is calculated numerically by solving

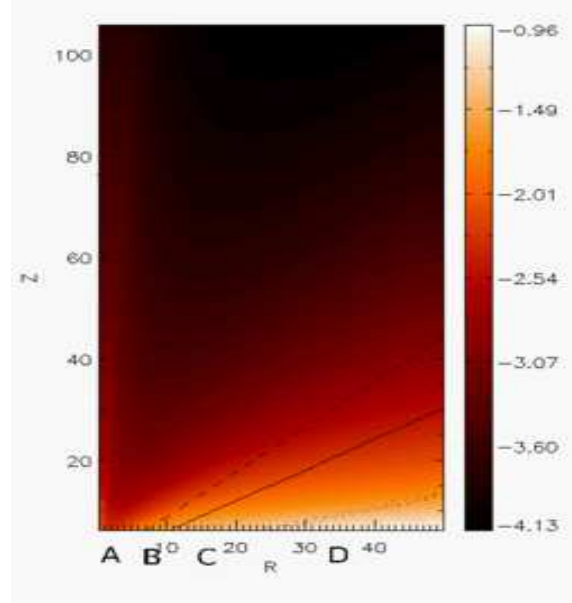


**Figure 1.** Initial conditions in our simulations, with marked inner-Z boundary regions of interest for the setup of boundary conditions. To avoid reflection from the outer-R boundary, we actually set our computational box three times larger in R-direction, and then analyze results only in the  $R \times Z = (128 \times 256)R_0$  portion of the domain. If not stated otherwise, all the results in this paper are shown at such resolution. In all the plots, the density is shown in a logarithmic color scale, and the three critical surfaces are plotted in dashed, solid and dotted lines, for fast magnetosonic, Alfvén and slow magnetosonic waves, respectively. Labels A, B, C and D mark portions of the inner-Z boundary where the flow is super-fast magnetosonic, super-Alfvénic, super-sonic and sub-sonic, respectively.

the first-order ordinary differential equations. After ensuring that the flow crosses the three singular MHD surfaces, by applying the appropriate regularity conditions (Vlahakis et al. 2000), the solution free parameters are chosen by following the Blandford & Payne (1982) choice, for easier comparison.

The magnetic diffusivity  $\eta$  we included in the simulations as a constant in the whole domain and normalized as

$$\eta = \hat{\eta} V_0 R_0 = \hat{\eta} \sqrt{\mathcal{G}\mathcal{M}R_0}/\kappa, \quad (11)$$

with dimensionless  $\hat{\eta}$ .

The self-similar solution breaks down near the rotation axis and the analytical solution of Vlahakis et al. (2000) is not provided for  $\theta$  smaller than 0.025 rad, measured from the axis. To perform numerical simulations in a computational box with the symmetry axis included, we modified the analytical solution<sup>1</sup>.

To maintain the divergence-free magnetic field as given by Eq. (7) with the extrapolated functions  $G$  and  $\psi$ , the initial magnetic field has to be modified. This is why, instead of using Eq. (7), we compute the  $B_Z$  component from the  $\hat{Z}$  component of the self-similar expression

<sup>1</sup> In this modified solution, results for  $\theta$  smaller than 0.025 rad, measured from the axis, are also missing. We linearly extrapolated it for the tabulated functions  $G, M$  and  $\psi$ . Modification of the functions  $G$  and  $M$  also means that the pressure/energy is modified near the axis.

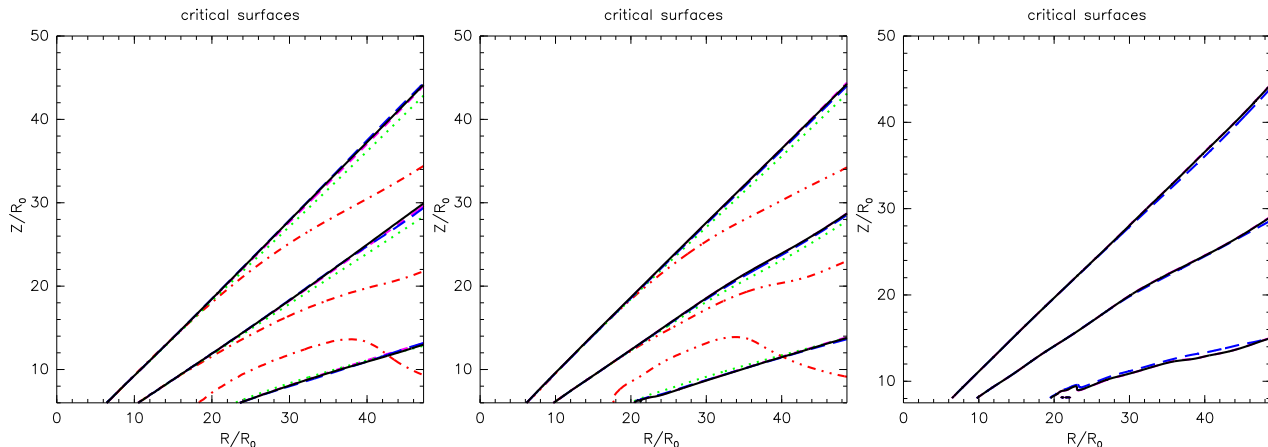


**Figure 2.** To estimate the numerical resistivity, we compare positions of the critical surfaces in  $R \times Z = (64 \times 128)$  grid cells,  $R \times Z = (128 \times 256)$  grid cells and  $R \times Z = (384 \times 768)$  grid cells in a  $(50 \times [6, 106])R_0$  part of the computational box in the *Left*, *Middle* and *Right* panels, respectively. Shown is only half of the computational box in the  $Z$ -direction, containing the critical surfaces. We show fast magnetosonic, Alfvén and slow magnetosonic critical surfaces positioned from higher to lower positions in the box, respectively. Solid (black), short-dashed (magenta), long-dashed (blue), dotted (green) and dot-dot-dot-dashed (red) lines show the quasi-stationary states (all at  $T=150$ ) for  $\eta = 0.0003, 0.003, 0.03, 0.15$  and  $1.5$ , respectively. In the rightmost panel we show results only for  $\eta < 0.1$ . From inspection of these results it follows that the level of numerical resistivity in  $R \times Z = (64 \times 128)$  and  $(128 \times 256)$  grid cells is about 0.1, and in the  $R \times Z = (384 \times 768)$  grid cells the numerical resistivity is about 0.01.

$$\mathbf{B}_p = \frac{B_0 R_0^2}{x} \nabla \times \left( \alpha^{x/2} \frac{\hat{\phi}}{R} \right), \quad (12)$$

and the component  $B_R$  from  $\nabla \cdot \mathbf{B}_p = 0$ , with boundary condition  $B_R(R=0) = 0$ . This procedure also requires the modification of the poloidal velocity, to obtain  $\mathbf{V}_p \parallel \mathbf{B}_p$  of the steady initially ideal-MHD flow. We compute the new direction of the poloidal initial velocity, maintaining the speed. For the cases with included physical resistivity, such a constraint will not be valid after the initial moment, which we set by ideal-MHD requirements.

Boundary conditions are the symmetry along the rotation axis, which is the inner,  $R_{\min}$  boundary, and out-flow conditions along the outer  $R$  and  $Z$  boundaries. At the  $Z_{\min}$  boundary we need to constrain only one quantity<sup>2</sup>. A detailed description of the boundary conditions is given in Matsakos et al. (2008). In Figure 1 we show regions A, B, C, D where  $V_Z > V_{Z,fast}$ ,  $V_{Z,fast} > V_Z > V_{Z,Alf}$ ,  $V_{Z,Alf} > V_Z > V_{Z,slow}$  and  $V_Z < V_{Z,slow}$ , respectively. Of eight boundary conditions for eight physical quantities (density, pressure, and three components for each of velocity  $V_R, V_\varphi, V_Z$  and magnetic field  $B_R, B_\varphi, B_Z$ ), one for magnetic field is determined by the  $\nabla \cdot \mathbf{B} = \nabla \cdot \mathbf{B}_p = 0$ . Of the remaining seven, three are determined from the computational box, by linear extrapolation to the ghost zone after crossing the three magnetosonic critical surfaces. This is because the number of boundary conditions is reduced by one for each critical surface which is crossed downstream, since the corresponding magnetosonic waves can not propagate outwards along the flow from those surfaces. We tried various combinations of quantities which are extrapolated and which are not. The one in which we could obtain sim-

ulations with the same setup for all the  $\eta$ , which enables a good comparison between the results, is the one with the  $R$ -component of velocity and the  $Z$ -component of the magnetic field extrapolated in portion B of the boundary. In addition to those two, in the portion A of the boundary, we extrapolate the toroidal component of the magnetic field from the computational box to the boundary.

Such a choice of boundary conditions still leaves us with over-specified boundary conditions, but this was the best combination we could obtain through the whole parameter space. For some values of  $\eta$ , simulations could be performed with the boundary conditions chosen closer to strict mathematical demands, but not for all the resistivities presented here. For a study of the dependence of the solutions on large resistivity, we needed a set of simulations in which we could investigate the same solution with an increasing parameter  $\eta$ .

In our computations we used various resolutions and sizes for the computational domain. Here we present the results for a resolution  $R \times Z = (128 \times 256)$  grid cells =  $([0, 50] \times [6, 106])R_0$ , in the uniform grid. Results comply with the solutions for one quarter, one half and double of this resolution, which we also computed for verification. In our results we show only the  $([0, 50] \times [6, 106])R_0$  part of the domain, but computations were performed with a three times longer domain in the radial direction,  $R \times Z = (384 \times 256)$  grid cells =  $([0, 150] \times [6, 106])R_0$ . The reason is that we preferred not to additionally specify the outer boundary to avoid artificial collimation as described in Ustyugova et al. (1999). We avoided doing so because in the case of large resistivity we do not have any clue about the solution. Instead, we extended the computational domain threefold in the radial direction. We take the result before any bounced wave from the outer- $R$  boundary would reach a part of the domain inside the  $([0, 150] \times [6, 106])R_0$ . It turned out that in simulations with very large resistivity the magnetic field does not collimate, and artificial collimation is not an issue.

<sup>2</sup> In C08 we fixed the boundary values for six physical quantities, to maintain the constant magnetic flux along the  $Z_{\min}$  boundary, while in Gracia et al. (2006) the boundaries were numerically over-specified, with 7 of them defined by the initial values.

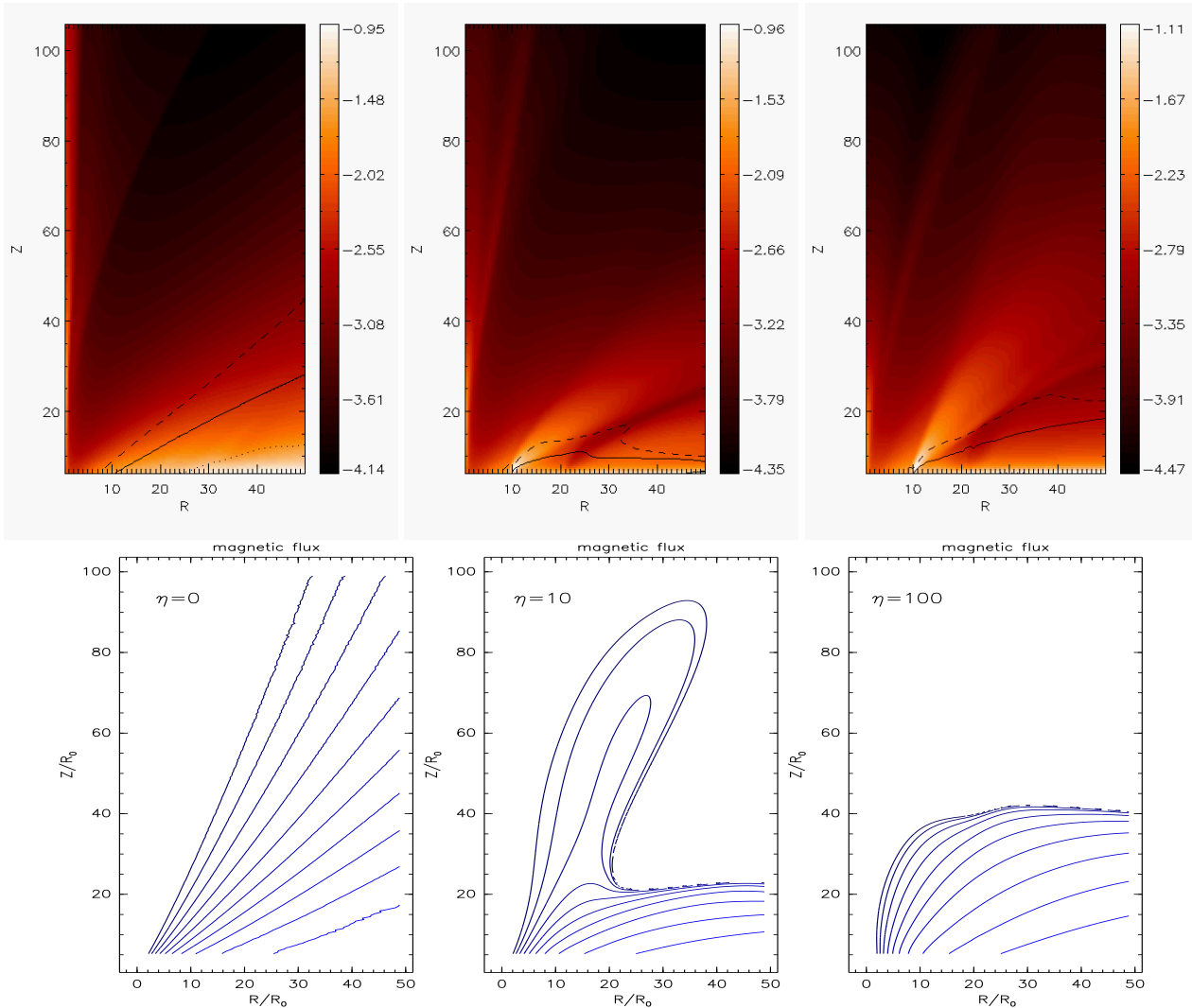


**Figure 3.** Illustration of the effect of resistivity on the density in the outflow. *Top panels:* In the *Left* panel are shown the quasi-stationary state solutions in the ideal-MHD case, and in the *Middle* and *Right* panels are shown solutions with large and very large resistivity,  $\eta = 10$  and  $100$ . Solutions with small resistivity are very similar to the ideal-MHD solution. Definitions of colors and lines are the same as in Figure 1. The obtained outflow for large and very large resistivity is supersonic in the entire domain, so that the slow magnetosonic surface is not present in those cases. *Bottom panels:* Magnetic flux isocontour lines with the above resistivities,  $\eta = 0, 10, 100$  in the *Left*, *Middle* and *Right* panels, respectively. Contours are parallel to the poloidal magnetic field lines. With a small  $\eta$ , magnetic flux isocontour lines are of the same geometry as for the ideal-MHD case. We obtain three different geometries of solutions for small, large and very large resistivity. The topology of the magnetic field lines for corresponding values of resistivity is always similar to one of the three modes shown.

Here we give a summary of our PLUTO code setup. We used cylindrical coordinates, an ideal equation of state, and the “dimensional splitting” option, which uses the Strang operator splitting to solve the equations in multiple dimensions. We checked if this introduces any difference, and found that in our problem the results are not affected by this choice. The spatial order of integration was set to “LINEAR”, meaning that a piecewise TVD linear interpolation is applied, accurate to second order in space. We used the second order in time Runge Kutta evolution scheme RK2, and for constraining the  $\nabla \cdot \mathbf{B} = 0$  at the truncation level, we chose the Eight-Waves option. Instead of a Riemann solver, we used a Lax-Friedrich scheme (“tvdlf” solver option in PLUTO).

## 2.2 Conserved integrals

It can be shown that steady, axisymmetric, ideal-MHD polytropic flows conserve five physical quantities along the poloidal magnetic field lines (Tsinganos 1982). Those so called *integrals* are the mass-to-magnetic-flux ratio  $\Psi_A$ , the field angular velocity  $\Omega$ , the total angular momentum-to-mass flux ratio  $L$ , the entropy  $Q$ , and the total energy-to-mass flux ratio  $E$  (we call the latter integral energy for brevity). They are given as

$$\Psi_A = \frac{4\pi\rho V_p}{B_p}, \Omega = \frac{V_\phi}{R} - \frac{B_\phi}{B_p} \frac{V_p}{R}, \quad (13)$$

$$L = RV_\phi - \frac{RB_\phi B_p}{\mu_0\rho V_p}, Q = p/\rho^\gamma, \quad (14)$$

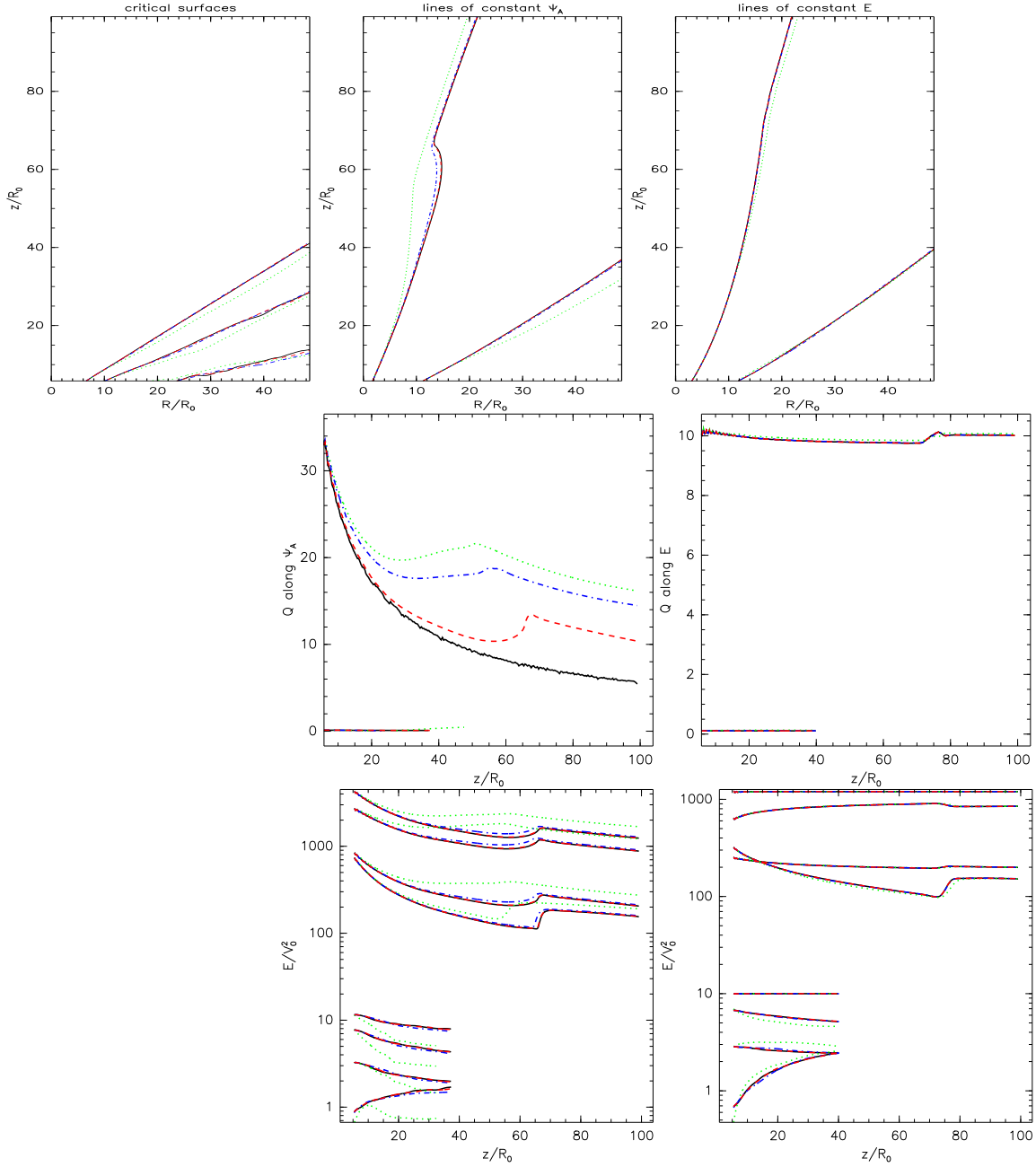


**Figure 4.** Illustration of the effect of small physical resistivity on the alignment of MHD integrals and magnetic flux surfaces. In the *Top Left* panel we show critical surfaces in the outflow with the resistivities  $\eta = 0, 0.01, 1$  and  $1.5$  shown in solid (black), dashed (red), dot-dashed (blue) and dotted (green) lines, respectively. The last value is shown to illustrate the difference in comparison with solutions above the critical value of  $\eta_c = 1.0$ . The Fast magnetosonic, Alfvén and slow magnetosonic critical surfaces are positioned from higher to lower positions in the box, respectively. In the *Top Middle* and *Top Right* panels are shown the shapes of two different poloidal magnetic field lines and energy integral isocontour lines along which we compute quantities shown in the panels in the rows below (shown with the same line type and color as in the plot of critical surfaces). As an example of the MHD-integrals, in the *Middle* panels we show the entropy  $Q$  along those lines, normalized to its value at large distance. In the *Bottom* panels we show a split-down of the energy contributions along the same two lines. In both panels the upper set of curves corresponds to the inner flux line, and the lower set of curves to the outer flux line. The color code of the lines is for the resistivities as above. The different line types now represent energy  $E$  (*solid*), kinetic energy (*dotted*), enthalpy (*dot-dashed*) and Poynting flux energy (*dashed*). The gravitational energy is not shown as it is orders of magnitude smaller.

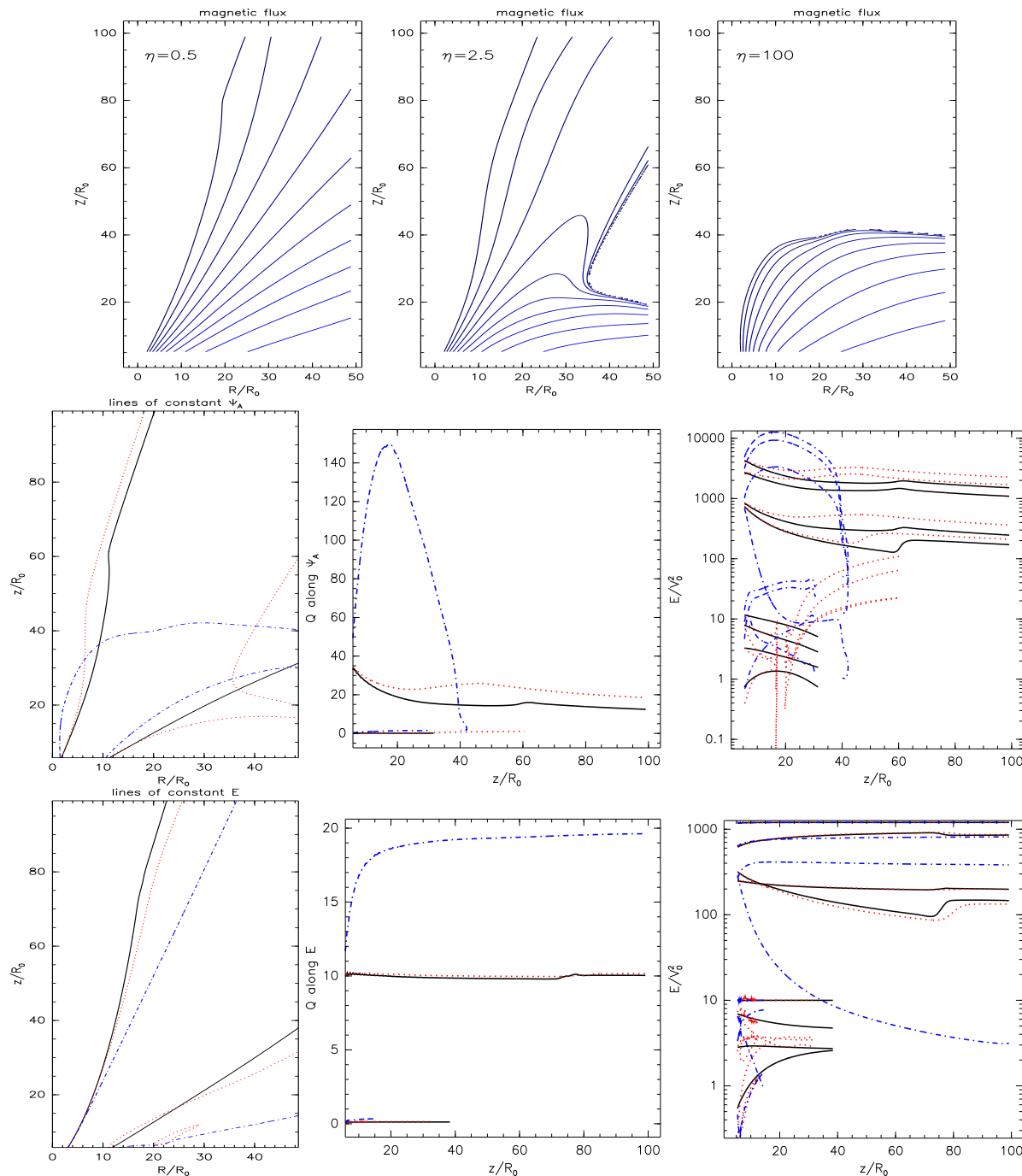


**Figure 5.** Illustration of the effect of small, large and very large physical resistivity on the magnetic field lines and alignment of MHD integrals and magnetic flux surfaces. In the *Top* panels are shown shapes of magnetic flux isocontour lines (which are parallel to the poloidal magnetic field lines) in a quasi-stationary state in simulations with  $\eta = 0.5, 2.5, 100$  in the *Left*, *Middle* and *Right* panels, respectively. In the *Middle* and *Bottom* panels, the *Left* panels show different poloidal magnetic field and energy integral isocontour lines along which quantities in the panels to their right are computed, for each resistivity. Legend of the figures is the same as in Figure 4.

$$E = \frac{V^2}{2} + \frac{\gamma}{\gamma - 1} \frac{P}{\rho} + \frac{B_\phi (B_\phi V_p - B_p V_\phi)}{\mu_0 \rho V_p} - \frac{GM}{r}. \quad (15)$$

The various contributions of the energy  $E$  correspond to the various terms on the right hand-side of the equation. From left to right, the kinetic, enthalpy, Poynting, and gravity terms can be recognized.

The degree of alignment of the lines on the poloidal plane where the above quantities are constant together with

the poloidal magnetic field lines can be used as a test how close to a steady-state the final result of a simulation is.

### 3 NUMERICAL RESISTIVITY

To investigate the effect of physical resistivity, it is necessary at first to estimate the effect of *numerical* resistivity. We

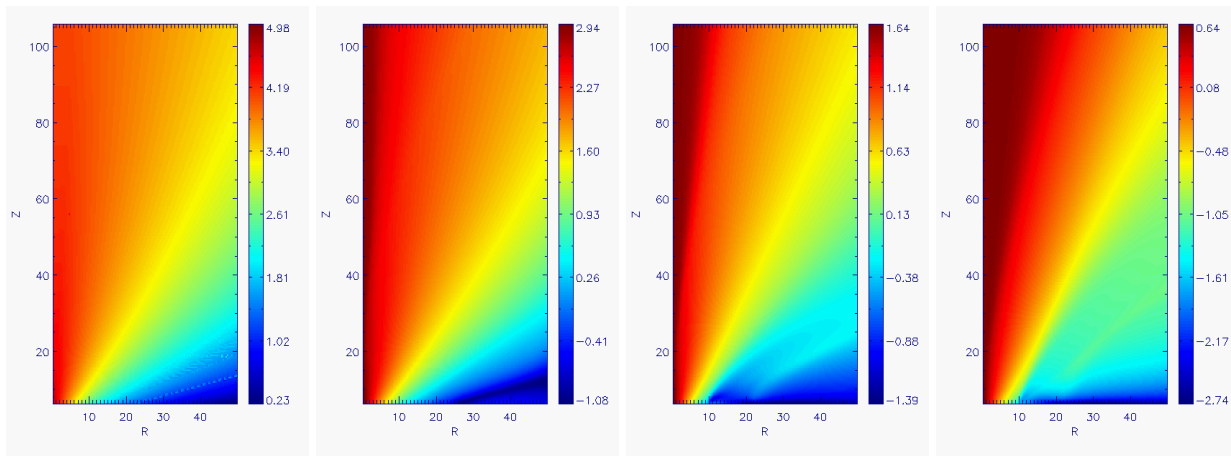


**Figure 6.** Reynolds magnetic number  $Rm = V\Delta x/\eta$  in the case of initial conditions, small, large, and very large physical resistivity, shown in the logarithmic color grading. *Left to Right* panels show  $Rm$  for  $\eta = 0.01, 0.5, 10$  and  $100$ , respectively. The numerical resistivity,  $\eta = 0.01$  is plotted at  $T=0$ , for easier comparison of the other values of  $\eta$  to the solution from Vlahakis et al. (2000).

check the level of numerical resistivity by comparing the simulations with decreasing parameter  $\eta$  until there is no effect on the solutions. For simplicity, we choose the over-specified boundary conditions setup, as was the case in C08. For small resistivities results are very similar to the results with the proper number of boundary conditions specified. Our results are presented in Figure 2.

The numerical resistivity is estimated as  $\eta = \Delta x^2/\tau$ , where  $\Delta x$  and  $\tau$  are the characteristic grid cell dimension and the characteristic time scale of the physical process, in this case diffusion of magnetic field. For the same  $\tau$ , the difference in numerical resistivity is then dependent on the second power of difference in grid cell dimensions. Explicitly, for grid cells of dimensions  $\Delta x_1$  and  $\Delta x_2$ ,  $\eta_1/\eta_2 = \Delta x_1^2/\Delta x_2^2$ . This means that for  $\Delta x_2 = 0.5\Delta x_1$  and  $\eta_1/\eta_2 = 0.25$  the numerical resistivity would be of the same order, and no clear difference could be observed. In consequence, it is not enough to just double (or half) the resolution, as is usually done, to check the effects of resistivity, one has to go further. Only for  $\Delta x_2 = 0.25\Delta x_1$  do we obtain  $\eta_1/\eta_2 = 0.06$ , with the numerical resistivity now different by an order of magnitude, the effect should be clearly visible.

One can not easily find a nontrivial problem with such a well defined stationary solution to compare this relation for numerical resistivities including all the terms in the MHD equations. An estimate of numerical resistivity follows the theoretical prediction, that its effects are visible only for a quadruple change in resolution. Our problem is well suited for such a check. We verified this prediction using our simulations in the low-resistivity range of physical resistivity. The procedure we described here could be used as a standard test for resistive MHD codes.

#### 4 RESULTS WITH PHYSICAL RESISTIVITY

The case of small resistivity has been investigated in C08, with the NIRVANA code. With large resistivity, we obtained a departure from the smooth pattern but, because of computational restrictions, we could not address it. As we have changed the code for our computations, we can now check

the previously obtained results. We investigate in detail what happens after the departure of the solution from the smooth pattern of change in the position of critical surfaces and integrals of motion.

In the simulations presented here, the computational box extends three times further in radial direction than the length of the portion of the box which we analyze. Therefore, we can control, and be certain that any information eventually traveling back towards the origin from the outer-R boundary did not reach the portion of the domain in which we are interested. All the simulations reach the quasi-stationary state before the disturbance from the outer boundary reaches back into the  $R=[0,50]$  part of the box.

##### 4.1 Results with small resistivity

As the first step in our simulations, we check if the setup in the PLUTO code gives the same trend observed previously in C08, with the smoothly increasing departure of integrals of motion from the ideal-MHD case for increasing resistivity. In Figure 4 we show the positions of the critical surfaces for the diffusivity  $\eta=0, 0.01, 1.0$  and  $1.5$ . The critical  $\eta$  we identify as  $\eta_c = 1$ . From the results obtained we conclude that the trend observed in previous simulations by the NIRVANA code holds also in the PLUTO results. With increasing resistivity, the change in the integrals of motion and the positions of critical surfaces are uniform and small. When reaching some critical resistivity,  $\eta_c = 1.0$ , the solutions still largely resemble the initial setup in the geometry of the magnetic field, but the critical surfaces and integrals of motion step out of the smooth pattern seen for the smaller values of  $\eta$ . An illustration of this is shown in Figure 4. In the bottom panels of Figure 3 is shown the transition in geometry between the solutions for small and large resistivity. This is an essential piece of information, since results like these trends of change are directly comparable only inside the same geometry. For the very different geometries we should compare only more general, non-local trends.

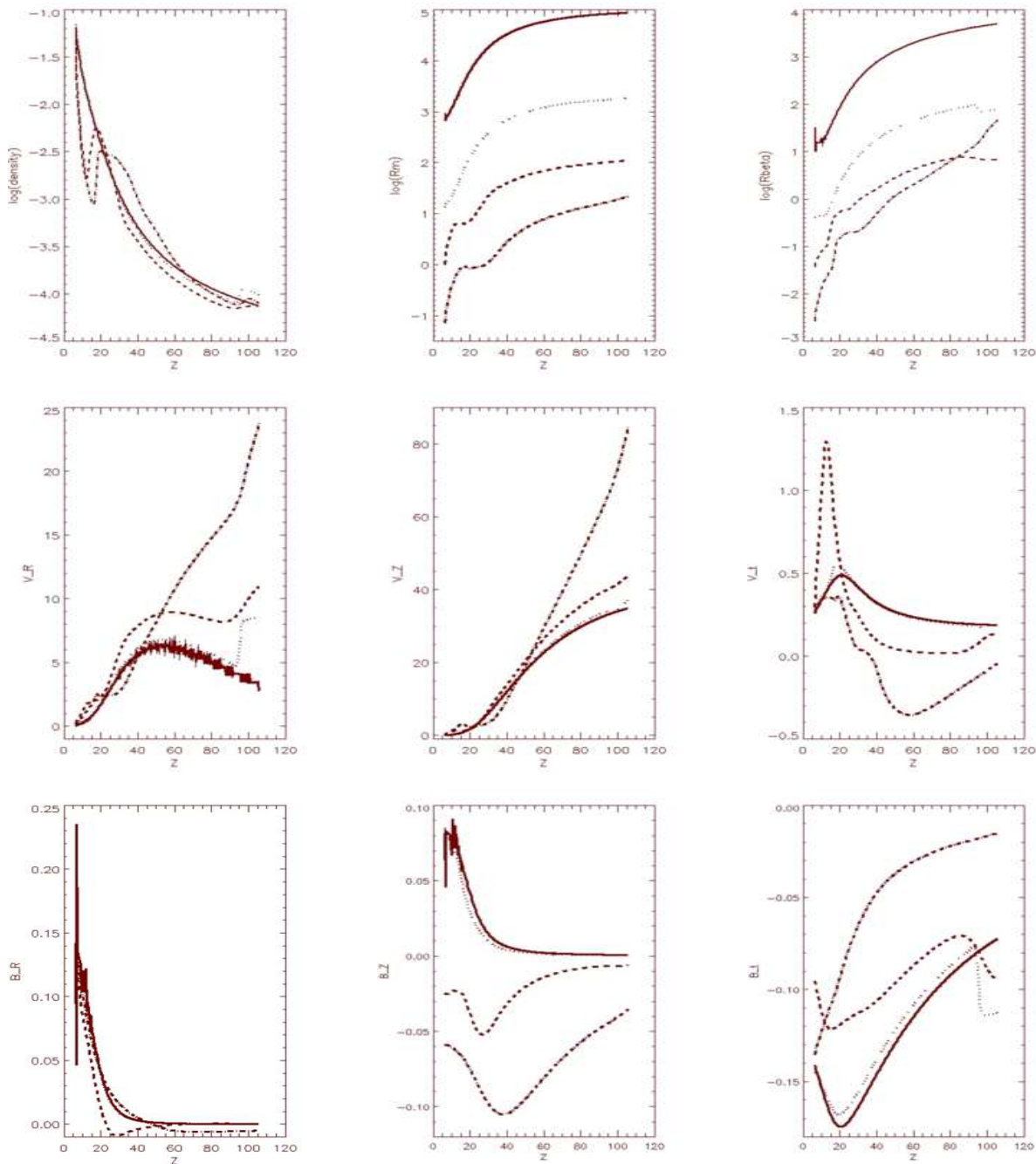


**Figure 7.** Various quantities computed along the slice parallel to the symmetry axis, at half of the computational box ( $R=25$ ). In solid, dotted, dashed and dot-dashed lines for  $\eta = 0.01, 0.5, 10$  and  $100$  are shown density, Reynolds magnetic number and  $R_\beta = \mu_0 R m P / B^2$  in logarithmic scale, and  $R, Z$  and toroidal components of velocity and magnetic field, respectively.

## 5 RESULTS WITH LARGE AND VERY LARGE RESISTIVITY

With resistivities approaching  $\eta = 1$ , the geometry of the solutions for the magnetic field lines starts to change. The value of  $\eta = 1$  is a critical value for this change, as it is where the smooth trend described in the previous subsection no longer applies in the whole box, because of the changed geometry. The typical solution in this second mode of geometry for a radially self-similar setup is shown in the middle pan-

els of Figure 3. The magnetic field “bulges” in the super-fast magnetosonic portion of the flow, and is compressed towards the meridional plane at large radial distances.

With even larger resistivities, approaching  $\eta = 10$ , the magnetic field geometry drastically changes once again. The “bulge” acquired with large resistivities is smoothed out, and only the compressed part of the field above the disk surface remains. This third mode of geometry for a radially self-similar setup is shown in the *Right* panels of Figure 3. There is no longer any collimation of the magnetic field. This



mode of the solution is stationary, it does not change further with an increase in resistivity. The largest value of resistivity for which our code still could run to a quasi-stationary state was of the order of a few hundreds.

Figure 6 shows the Reynolds magnetic number in our computational box in simulations with increasing  $\eta$ . The profile of  $R_m$  traces the increasingly de-collimating outflow, indicating that the resistivity is directly related to the geometry of the magnetic field. In Figure 7 we show various quantities along the slice parallel to the axis of symmetry, at half the computational box, for the full range of  $\eta$  considered in this work. The density does not differ much in our solutions. Poloidal velocity increases for large and very large resistivities. Rotation changes direction for very large resistivities.  $B_z$  also changes direction for large and very large resistivities, but it is interesting that  $B_R$  changes direction only for large, but not for very large resistivities.

In Čemeljić et al. (2008) we estimated the physical magnetic diffusivity in the astrophysical case of young stellar object with solar mass  $M \approx M_\odot$  and with a characteristic distance of  $0.1AU = 1.4 \times 10^{10}m$ . Here we extend it to the increased range of diffusivity. From Eq. (11), for the diffusivities  $\hat{\eta} = (1, 10, 100)$  in the code units, we obtain the physical diffusivities  $\eta = (1, 10, 100) \times 6.8 \times 10^{14}m^2s^{-1} = (1, 10, 100) \times 6.8 \times 10^{18}cm^2s^{-1}$ , respectively.

## 6 SUMMARY

We obtained solutions of resistive-MHD self-similar outflows above the accretion disk for the regimes of small, large and very large resistivities. The disk is not included in the simulations, but is taken as a boundary condition.

To find the lower limit of small resistivity, we first find the level of numerical resistivity. We also verified the predicted behavior of numerical resistivity with increasing grid resolution: it is not enough to double the grid resolution to obtain the decrease in numerical resistivity for an order of magnitude. One has to quadruple the number of grid cells. A similar procedure could be used as a standard test for resistive MHD codes.

Next we verified the solutions from our previous work in C08, for small resistivity, since there we used a different code. We find the same trend. Since now we have a parallel code, we can investigate solutions with larger resistivities. Solutions with small, large and very large resistivities each have a different geometry, so that we can distinguish three modes of solutions.

The first mode is similar to the ideal-MHD solutions. With  $\eta > 1$ , there appears a “bulge” in the magnetic field, which is a signature of the second mode. At even larger resistivities, with  $\eta > 10$ , the third mode of solutions sets in. In the third mode, the magnetic field is no longer collimated, but is pressed towards the disk. Such a solution does not change further with increasing resistivity.

## 7 ACKNOWLEDGMENTS

MČ completed this work in the Theoretical Institute for Advanced Research in Astrophysics (TIARA) under contract funding by Theoretical Institute for Advanced Research in

Astrophysics (TIARA) in the Academia Sinica and National Tsing Hua University through the Excellence Program of the NSC, Taiwan. Simulations have been initially performed during MČ stay in Athens at spring 2009, supported by the European Community’s Marie Curie Actions - Human Resource and Mobility within the JETSET (Jet Simulations, Experiments and Theory) network under contract MRTN-CT-2004005592. Fruitful discussions with Ruben Krasnopolsky are acknowledged, and we thank A. Mignone for possibility to use the PLUTO code. MČ thanks to M. Stute for help with PLUTO setup, and J. Gracia for his python scripts for some of the plots.

## REFERENCES

- Blandford R. D., Payne D. G., 1982, MNRAS, 199, 883  
 Čemeljić M., Gracia J., Vlahakis N., Tsinganos K., 2008, MNRAS, 389, 1022 (C08)  
 Gracia J., Vlahakis N., Tsinganos K., 2006, MNRAS, 367, 201 (GVTO6)  
 Matsakos T., Tsinganos K., Vlahakis N., Massaglia S., Trussoni E., 2008, A&A, 477, 521  
 Mignone A., Bodo G., Massaglia S., Matsakos T., Tesileanu O., Zanni C., Ferrari A., 2007, ApJS, 170, 228  
 Tsinganos K., 1982, ApJ, 252, 775  
 Ustyugova G. V., Koldoba, A. V., Romanova, M. M., Chechetkin V. M., Lovelace R. V. E., 1999, ApJ, 516, 221  
 Vlahakis N., Tsinganos K., 1998, MNRAS, 298, 777  
 Vlahakis N., Tsinganos K., Sauty C., Trussoni E., 2000, MNRAS, 318, 417  
 Ziegler U., 1998, Comput. Phys. Commun., 109, 111

This paper has been typeset from a  $\text{\TeX}/\text{\LaTeX}$  file prepared by the author.